THE JOURNAL OF PHYSICAL CHEMISTRY C
A JOURNAL OF THE AMERICAN CHEMICAL SOCIETY

pubs.acs.org/JPCC
Article

Polymorph-Induced Reducibility and Electron Trapping Energetics of Nb and W Dopants in TiO_2

Amit Chaudhari, Andrew J. Logsdail, and Andrea Folli*

Cite This: J. Phys. Chem. C 2025, 129, 15453−15461

Read Online

ACCESS | Metrics & More | Article Recommendations | Supporting Information

ABSTRACT: Controlling the formation of electron polarons in TiO_2 doped with transition metals is important for the design of transparent conducting oxides for high-efficiency photovoltaics and photocatalysts with tunable reaction selectivities. In this work, EPR spectroscopy is combined with Hubbard-corrected density functional theory (DFT+U), with refined atomic-like Hubbard projectors, to show the sensitivity of charge compensation in substitutionally doped Nb-TiO_2 and W-TiO_2 with respect to the TiO_2 polymorph (*i.e.*, anatase or rutile). Both EPR magnetic tensors and DFT+U-predicted Nb 4*d* and W 5*d* orbital occupancies show the formation of differing dopant charge states depending on the TiO_2 polymorph, with nonmagnetic Nb^{5+} and W^{6+} in doped anatase and paramagnetic Nb^{4+} and W^{5+} in doped rutile. The results provide an example of how a coherent experimental and theory-validated framework can be used to understand and predict the reducibility of dopants and electron trapping energetics in TiO_2 polymorphs. The outcome enables greater control over the electronic and magnetic properties of metal oxide semiconductors, which are crucial for the rational design of next-generation materials for energy conversion and catalytic applications.

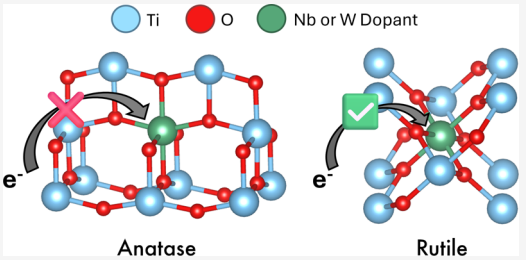

1. INTRODUCTION

Transparent conducting oxides (TCOs) underpin modern consumer electronics, photovoltaics, and light-emitting devices (LED and OLED). For example, anatase Nb-doped TiO_2 (NTO) has emerged[1−10] as a more sustainable alternative to the widely used indium tin oxide,[11−14] capable of a resistivity of 2×10^{-4} to 3×10^{-4} Ωcm and 97% internal transmittance under visible light at room temperature for a 40 nm-thick film of anatase NTO with $3\%_{at}$ Nb.[1] In contrast, rutile NTO is more resistive,[2] which allows for tailored applications based on the choice of TiO_2 polymorph. Similarly, anatase W-doped TiO_2 (WTO) exhibits an n-type metallic behavior[15,16] with a resistivity of 1.5×10^{-2} Ωcm at room temperature for films with a doping concentration of $6.3\%_{at}$.[15] WTO has potential for TCO applications in electron transport layers in perovskite solar cells, with a demonstrated efficiency 28× greater than undoped TiO_2.[17] NTO and WTO have also attracted attention as promising photocatalysts with a 65% increase in photocurrent demonstrated for NTO nanorod photoelectrodes doped with $0.25\%_{at}$ Nb when compared to undoped TiO_2.[18] NTO nanostructures, ranging from rutile nanorods to anatase nanosheets, also show improved adsorption of molecular O_2 and the formation of superoxide radicals $O_2^{\cdot-}$ under irradiation when compared to pristine TiO_2 with the same morphology.[19] Furthermore, both NTO and WTO nanostructures show enhanced dye photodegradation,[20,21] photooxidation of nitrogen oxides (NO_x) to nitrates,[22] and ozone gas sensing[20] when compared to undoped TiO_2.

To understand and further optimize the performance of NTO and WTO, it is necessary to characterize and model the behavior of electrons and holes that contribute to material conductivity and chemistry. This includes the mobility of charge carriers within the bands (conduction and valence, respectively), their recombination, their trapping (forming electron polarons), and the charge carrier transfer mechanisms that drive redox processes when these materials are used as semiconductor photocatalysts. Given the electronic spin associated with electrons and holes, electron paramagnetic resonance (EPR) spectroscopy is a powerful tool for the precise identification and characterization of the dynamics, lifetimes, and spatial distribution of excitons and their trapping states within NTO and WTO, including the paramagnetic species following insertion of Nb and W dopants in the TiO_2 lattice. For example, electron trapping states are mostly associated with Nb^{4+} and W^{5+} species, which are both paramagnetic d^1 species that can be detected and interrogated by EPR spectroscopy. The formation of Nb^{4+} and W^{5+} versus *vs.* Nb^{5+} and W^{6+} is particularly important as it directly influences conductivity and photocatalytic efficiency.

Received: June 24, 2025
Revised: July 27, 2025
Accepted: July 31, 2025
Published: August 19, 2025

https://doi.org/10.1021/acs.jpcc.5c04364
J. Phys. Chem. C 2025, 129, 15453−15461

The literature is conflicted with respect to the lack of Nb^{4+} and W^{5+} EPR signals when substitutional Nb and W are introduced in anatase TiO_2, in contrast to the presence of Nb^{4+} and W^{5+} EPR signals in doped rutile TiO_2. There is currently no clear explanation of this observation, and so far, first-principles atomistic modeling methods like density functional theory (DFT) have not completely clarified these experimental observations. For example, geometry optimization with semilocal DFT followed by a single point calculation using a screen exchange hybrid functional (sX) predicts shallow donor states that are largely delocalized over Ti sites in anatase NTO,[5] supporting resonant photoemission experiments, which confirm the absence of midgap states for anatase NTO.[2,23] However, the same DFT calculations also predict a deep localized state in rutile NTO that is 0.9 eV below the conduction band edge, involving Ti $3d_{xy}$ orbitals with a small contribution from Nb 4*d* orbitals, thus contradicting the EPR observations.[5] Hubbard-corrected density functional theory (DFT+*U*) calculations predict Ti 3*d* midgap states in rutile NTO,[24] but reports vary, with some predicting shallow donor states in rutile NTO[25] and deep Ti 3*d* states in both anatase NTO[25,26] and anatase WTO,[26] *i.e.*, contradicting results. These computational results, based on DFT+*U* using planewave basis sets, fail to provide an unambiguous interpretation/prediction of the experimental observations; however, hybrid-DFT has been demonstrated to successfully predict W 5*d* midgap states in rutile WTO when using all-electron atom-centered basis functions to describe the wave function near the nucleus (in the full-potential linear augmented plane wave approach), and this gives promise for application of alternative basis representations.[27]

In this work, experimental EPR spectra for powder anatase and rutile NTO and WTO are presented, including the magnetic tensors characterizing Nb^{4+} and W^{5+} polarons in doped rutile, alongside DFT+*U* simulations in an all-electron numerical atom-centered orbital (NAO) framework[28] to successfully simulate the experimental EPR observations. The DFT+*U* simulations use a refined atomic-like Ti 3*d* Hubbard projector, as well as the "*occupation matrix control*" (OMC) method,[29] for controlling the Ti 3*d*, Nb 4*d*, and W 5*d* orbital occupancies through the self-consistent optimization of the system electronic structure towards the ground state. The presented combination of experiment and theory improves our fundamental understanding of the nature and formation of reduced species in semiconductor metal oxides, enabling the rational design of superior TCOs and heterogeneous photocatalysts.

2. METHODOLOGY

2.1. Material Synthesis. The NTO and WTO materials studied in this work were synthesized *via* a sol−gel route. 10 mL of titanium isopropoxide (≥97%, Sigma-Aldrich) was dissolved in 10 mL of anhydrous ethanol. After thorough mixing, 5 mL of deionized water (18 MΩcm) was slowly added to the solution. The resulting white precipitate redissolved upon further stirring. In the next step, 20 mL of a pH 10 ammonia/ammonium chloride buffer (5% ammonia, Sigma-Aldrich) was added to the solution. Finally, the desired amount of ammonium tungstate (BDH Chemicals) or ammonium niobate (V) oxalate hydrate (BDH Chemicals) to achieve a nominal 0.1 or 1.0 atom % was dissolved in 10 mL of warm deionized water and subsequently added to the solution. After thorough stirring for at least 4 h, the solution was filtered, washed several times with deionized water, and then dried at 60 °C for 4 h. The dry powders were ground in an agate mortar and transferred into a crucible for calcination. The samples were calcined at 600 °C for 4 h and then ground again afterward.

2.2. Powder X-ray Diffraction. To confirm mineralogy and crystallinity, X-ray diffraction (XRD) patterns were obtained using a Bruker D8 Advance diffractometer equipped to deliver CuKα_1 X-ray radiation (1.54 Å) at room temperature. Refinement of the powder XRD patterns was carried out using the Profex suite for XRD.[30]

2.3. EPR Spectroscopy. X-band continuous-wave (CW) EPR spectra were recorded on a Bruker Elexsys E500 spectrometer equipped with an Oxford Instruments liquid-helium cryostat and a Bruker ER4122 SHQE-W1 superhigh Q resonator operating at 50 K. Before each measurement, the samples were evacuated for at least 12 h at 393 K and under a dynamic vacuum at ca. 1×10^{-4} bar. Experimental spectra were simulated using the EasySpin toolbox[31] for Mathworks Matlab.

2.4. Electronic Structure Calculations. *2.4.1. DFT.* All electronic structure calculations were performed using the Fritz-Haber Institute *ab initio* materials simulation (FHI-aims) software package,[32] which uses an all-electron NAO basis set, interfaced with the Python-based atomic simulation environment (ASE).[33] The standard light basis set (2020) was used, with equivalent accuracy to the TZVP Gaussian-type orbital basis set,[34] as decided after benchmarking the TiO_2 formation energy (see the Supplementary Information, SI, Section S1.1). Relativistic effects were accounted for using the zeroth-order regular approximation[32] as a scalar correction, while the system charge and spin were set to zero. Periodic boundary conditions were applied using converged **k**-point sampling for the optimized anatase and rutile unit cell, separately (see SI Section S1.1). The mBEEF meta-GGA exchange correlation functional was used,[35,36] as defined in Libxc,[37] providing the best balance of accuracy and cost compared to other local, semilocal, and hybrid functionals (see SI Section S1.1). Self-consistent field (SCF) optimization of the electronic structure was achieved using a convergence criterion of 1×10^{-6} eV for the change in total energy, 1×10^{-4} eV for the change in the sum of eigenvalues, and 1×10^{-6} e a_0^{-3} for the change in charge density. Geometry optimization used the quasi-Newton BFGS algorithm[38−41] with a force convergence criterion of 0.01 eV/Å. Point defect calculations were performed using a $3 \times 3 \times 3$ TiO_2 supercell containing 324 and 162 atoms for anatase and rutile, respectively. The supercell size avoids spurious long-range defect−defect interactions between periodic images while simulating at low defect concentrations of 0.308% (anatase) and 0.617% (rutile) following substitution of a Ti atom with a Nb or W atom. Defect energies were calculated as

$$\Delta E_{\mathrm{Defect}} = E_{\mathrm{DefectiveBulkTiO_2}} + \mu_{\mathrm{Ti}} - E_{\mathrm{StoichiometricBulkTiO_2}} - \mu_{\mathrm{Dopant}} \quad (1)$$

For these systems, the chemical potential μ was calculated using the energy of bulk Ti (hexagonal close-packed structure), Nb (body-centered cubic structure), and W (body-centered cubic structure). All defect energies are listed in SI Section S1.3.3.

2.4.2. DFT+U. All DFT+*U* calculations were performed using the on-site definition of the occupation matrix and the

https://doi.org/10.1021/acs.jpcc.5c04364
J. Phys. Chem. C 2025, 129, 15453−15461

fully localized limit double counting correction.[28] A Hubbard correction was applied to correct for the Coulomb self-interaction of Ti 3*d* orbital electrons only. Both the Hubbard *U* value and the occupation matrix ($\mathbf{n}_I^\sigma$), which contains orbital occupancies for every spin channel (σ) for every atom (I), are used to calculate the corrective Hubbard term (E_U^0) as[28]

$$E_U^0[\mathbf{n}_I^\sigma] = \sum_{(\sigma,I)} U^I[\mathrm{Tr}(\mathbf{n}_I^\sigma) - \mathrm{Tr}(\mathbf{n}_I^\sigma \mathbf{n}_I^\sigma)] \quad (2)$$

Once E_U^0 is calculated, the total energy of the system ($E_{\mathrm{DFT}+U}$) is calculated using the DFT+*U* Hamiltonian, where $\rho(\mathbf{r})$ is the electron density, E_{DFT} is the total energy of the system accounting for localized and delocalized orbitals, and E_U^{dc} prevents the double counting of localized states in both E_{DFT} and E_U^0:[28]

$$E_{\mathrm{DFT}+U}[\rho(\mathbf{r})] = E_{\mathrm{DFT}}[\rho(\mathbf{r})] + E_U^0[\mathbf{n}_I^\sigma] - E_U^{\mathrm{dc}}[\mathbf{n}_I^\sigma] \quad (3)$$

The occupation matrix is calculated by projecting all DFT-predicted Kohn–Sham states onto atomic-like orbitals defined by a Hubbard projector.[28] However, using the default atomic Ti 3*d* Hubbard projector presented challenges in identifying the ground-state electronic structures of anatase and rutile NTO and WTO due to numerical instability. Therefore, constrained and self-consistent DFT+*U* calculations were performed with an atomic and modified Ti 3*d* Hubbard projector, respectively. Constrained DFT+*U* calculations were performed using the default atomic Ti 3*d* Hubbard projector and a Ti 3*d* Hubbard *U* value of 3 eV in anatase TiO_2 and 4 eV in rutile TiO_2. These Hubbard *U* values were chosen to minimize the average error in the DFT+*U*-predicted band gap and unit cell equilibrium volume, calculated by fitting to the Birch–Murnaghan equation of state using ASE,[42] versus experimental references (see SI Section S1.2).[43,44] Here, the OMC method[29] was used to *fix* the polaron(s) at specific atom(s) by modifying the corresponding atomic orbital occupation matrix (see SI Section S1.3.1).

Next, self-consistent DFT+*U* calculations were performed with a refined atomic-like Ti 3*d* Hubbard projector. Here, the "*occupation matrix release*" method[28] was used to *initialize* the polaron(s) at specific atom(s) before a two-step optimization of the system electronic structure until full geometry optimization was achieved (see SI Section S1.3.1). A refined atomic-like Ti 3*d* Hubbard projector was defined as a linear combination of the atomic Ti 3*d* and hydrogenic auxiliary basis function in the light basis set, where the auxiliary function is subject to a Gram–Schmidt orthogonalization with respect to the atomic function, with the corresponding linear combination expansion coefficients $c_1 = 0.828$ and $c_2 = -0.561$. The values of c_1 and c_2 were chosen based on the work of Jakob and Oberhofer, who computed a Ti 3*d* Hubbard projector for bulk rutile TiO_2 in FHI-aims from first-principles.[45] These coefficients enabled successful convergence to the ground state using a Ti 3*d* Hubbard *U* value of 3 eV for both anatase and rutile NTO and WTO. In general, tuning the Hubbard projector in FHI-aims to navigate numerical instability in the simulation of defective transition metal oxides has not yet been systematically investigated and will be the focus of a future study.

3. RESULTS AND DISCUSSION

3.1. Polymorphism and Dopant Loadings. The refined X-ray powder diffraction patterns, presented in SI Section S2, show that 0.1%$_{\mathrm{at.}}$ Nb or W in TiO_2, synthesized *via* a sol–gel route and calcined at 600 K, allows for the formation of mixed anatase and rutile polymorphs. The same result occurs for undoped TiO_2, which exhibits a rutilization temperature higher than 500 K (calcination of sol–gel TiO_2 precursors with 0.1%$_{\mathrm{at.}}$ Nb or W at $T < 500$ K generates anatase-only polymorphs[9,46,47]). Refinement of the XRD patterns (SI Section S2) reveals 92% anatase and 8% rutile for NTO and 72% anatase and 28% rutile for WTO. These samples are referred to as NTO-AR and WTO-AR herein. On the contrary, 1.0%$_{\mathrm{at.}}$ of the same dopants in conjunction with calcination at 600 K allows for the formation of anatase-only NTO and WTO (SI Section S2). These samples are referred to as NTO-A and WTO-A herein.

3.2. Experimentally Detected Electron Trapping States in Anatase and Rutile NTO and WTO. Electron and hole trapping are normally single electron transfer events occurring within the material. As such, they can be followed experimentally by detecting the formation or disappearance of paramagnetic species using EPR spectroscopy. Nb^{5+} ($[Kr]4d^0$) and W^{6+} ($[Xe]5d^0$) replace Ti^{4+} ($[Ar]3d^0$) in the TiO_2 lattice aliovalently and isomorphically, as Nb^{5+}, W^{6+}, and Ti^{4+} have almost identical octahedral coordination environments with ionic radii of 78 pm, 74 pm, and 74.5 pm, respectively. The dopant incorporation reactions for extrinsic defects using the Kröger–Vink notation can be written as follows:

$$Nb_2O_5 \xrightarrow{2TiO_2} 2Nb_{Ti}^{\cdot} + 4O_O^x + 2e' + \frac{1}{2}O_2 \quad (4)$$

$$2Nb_2O_5 \xrightarrow{5TiO_2} 4Nb_{Ti}^{\cdot} + V_{Ti}^{''''} + 10O_O^x \quad (5)$$

$$WO_3 \xrightarrow{TiO_2} W_{Ti}^{\cdot\cdot} + 2O_O^x + 2e' + \frac{1}{2}O_2 \quad (6)$$

$$2WO_3 \xrightarrow{3TiO_2} 2W_{Ti}^{\cdot\cdot} + V_{Ti}^{''''} + 6O_O^x \quad (7)$$

Valence-induced electron formation, as highlighted by eqs 4 and 6, increases the n-type character of NTO and WTO compared to that of undoped TiO_2. Our EPR attempts at identifying *substitutional* and *isolated* Nb^{4+} and W^{5+} in NTO-A and WTO-A failed, which corroborates with previous experiments by De Trizio et al., which could not detect Nb^{4+} in Nb-doped colloidal anatase nanocrystals even at liquid-helium temperature.[6] Giamello and co-workers[8] and ourselves[9] independently showed that, in the case of Nb doping in anatase-only TiO_2, Ti^{3+} is mostly formed as a result of valence induction when Nb^{5+} aliovalently replaces Ti^{4+} in the anatase lattice:

$$Ti_{Ti}^x + e' \rightarrow Ti_{Ti}' \quad (8)$$

The resulting Ti^{3+} exhibits an anisotropic EPR spectrum characterized by a $\boldsymbol{g}$ tensor with axial symmetry and principal values equal to $g_\perp = 1.988$ and $g_{//} = 1.957$,[8,9] consistent with a highly delocalized bulk species that is responsible for causing an increased conductivity of the doped anatase TiO_2.[8] This Ti^{3+} is structurally and magnetically different from a surface-localized Ti^{3+} that forms following chemical or chemo/thermal reduction of undoped TiO_2.[8] The amount of delocalized bulk Ti^{3+} can also be augmented by photoinjection of extra conduction electrons[8,9] followed by trapping:

$$\gamma \xrightarrow{TiO_2} h_{vb}^+ + e_{cb}^- \quad (9)$$

https://doi.org/10.1021/acs.jpcc.5c04364
J. Phys. Chem. C 2025, 129, 15453–15461

The situation appears completely different in the cases of NTO-AR and WTO-AR, as demonstrated by the respective X-band CW EPR spectra reported in Figure 1a (NTO-AR) and Figure 1b (WTO-AR).

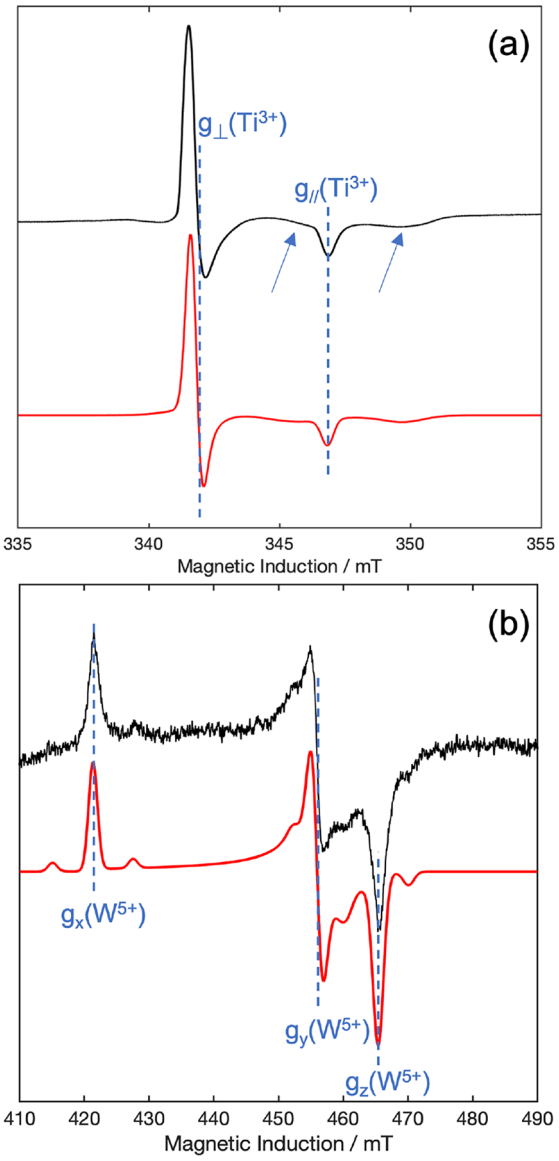

Figure 1. X-band CW EPR spectra at 50 K for (a) Nb-doped and (b) W-doped mixed-polymorph TiO_2 nanoparticles with a doping concentration of $0.1\%_{at.}$ (NTO-AR and WTO-AR, respectively).

The clear axial signal in the spectrum of NTO-AR in Figure 1a can be attributed to bulk Ti^{3+}, as previously described for the case of solely the anatase polymorph. A very broad and low-intensity signal is also visible at 50 K as shown by the arrows in Figure 1a. We propose that this broad signal is associated with Nb^{4+} in rutile. This assignment can be explained as follows. Figure 2b,c show the simulated angular dependency of the single-crystal EPR spectra at 4.2 K of Nb^{4+} centers in pure rutile NTO at the X- and Q-bands, respectively, computed using experimental values derived from a rutile single crystal.[48]

The crystal structure of rutile TiO_2 in Figure 2a is tetragonal (D_{4h}^{14}, space group P42/mnm) with two Ti per unit cell, which are equivalent except for a $\pi/2$ rotation about the c axis, as also evidenced by the orientation of the eigenframes of the magnetic tensors reported for the two inequivalent sites I and II in Figure 2a. The two Ti sites possess orthorhombic point symmetry D_{2h}. Details of the spin Hamiltonian used for the simulations can be found in Table 1.

The g_x and g_y completely overlap at X-band frequencies, but they can be resolved at Q-band frequencies. Hyperfine interaction of the $4d^1$ unpaired electron with the ^{93}Nb nucleus is expected ($I(^{93}Nb) = 9/2$, 100% natural abundance), giving rise to 10 hyperfine lines. The A_y value is noticeably larger than A_x and A_z, with some resolved structure due to $\delta m_I = \pm 1$ transitions that are allowed *via* the electric quadrupole interaction when **B** is not aligned to the principal axes of the crystal. The hyperfine structure has been shown to vanish above 25 K on the single crystal,[48] with particularly the **B**//[001] and **B**//[1$\bar{1}$0] sets of lines coalescing into a single line already at 25 K.[48] The increasingly dispersive character of the signal above 25 K and the line narrowing observed upon coalescing of the hyperfine structure were interpreted by Zimmermann[48] as a combination of two contributions, *i.e.*, thermal excitation of $4d^1$ donor electrons to the conduction band plus exchange scattering of $4d^1$ donor electrons with the conduction band. Both of these contributions give rise to electron hopping from different donor sites (*i.e.*, Nb^{4+}) via the conduction band (Anderson's model of random frequency modulation). The activation energy for the hopping between the donor level and the conduction band was found to be E_a/k = 72 K at temperatures below 40 K, while the same activation energy was much larger at temperatures up to 300 K, in agreement with more recent evidence suggesting that rutile NTO is resistive at room temperature.[2] Moving from single crystal to powder samples, Kiwi et al.[50] showed that, in a mixed anatase and rutile powder sample, a broad signal could be found at 4.2 K matching the g tensor reported by Zimmermann.[48] Our broad signal in Figure 1a matches the signal reported by Kiwi et al.,[50] although it is much broader due to the much higher temperature of our measurement, *i.e.*, 50 K (according to Zimmermann,[48] the signal completely vanishes above 77 K).

$$Nb_{Ti}^{\cdot} + e' \rightarrow Nb_{Ti}^{x} \tag{10}$$

In the case of WTO-AR, the situation is very similar to that described above for NTO-AR. Figure 1b shows a clear anisotropic EPR spectrum characterized by a rhombic g tensor with principal values reported in Table 1. Small intensity doublets ($m_I = \pm 1/2$ lines) are visible on each side of the three principal resonances due to hyperfine interaction of the $5d^1$ unpaired electron with the ^{183}W nucleus ($I(^{183}W) = 1/2$, 14.3% natural abundance). The other naturally occurring isotopes of W are ^{180}W, ^{182}W, ^{184}W, and ^{186}W, all with nuclear spin quantum number $I = 0$, and these account for the three principal $m_I = 0$ resonance lines. W^{5+} in TiO_2 is not affected by the same fast relaxation issues as Nb^{4+} and therefore well-defined EPR spectra can be easily obtained at 50 K, as visible in Figure 1b. The values of the magnetic tensors are in good agreement with those of Chang[49] for W^{5+} centers in rutile single crystals. The angular dependency has been simulated in Figure 2d,e at the X- and Q-bands, respectively.

This combined evidence of NTO-AR and WTO-AR indicates that the reduction of Nb^{5+} and W^{6+} dopants in the TiO_2 host lattice occurs only in the rutile polymorph.

3.3. Computed Electron Trapping States in Anatase and Rutile NTO and WTO. To rationalize the magnetic

https://doi.org/10.1021/acs.jpcc.5c04364
J. Phys. Chem. C 2025, 129, 15453−15461

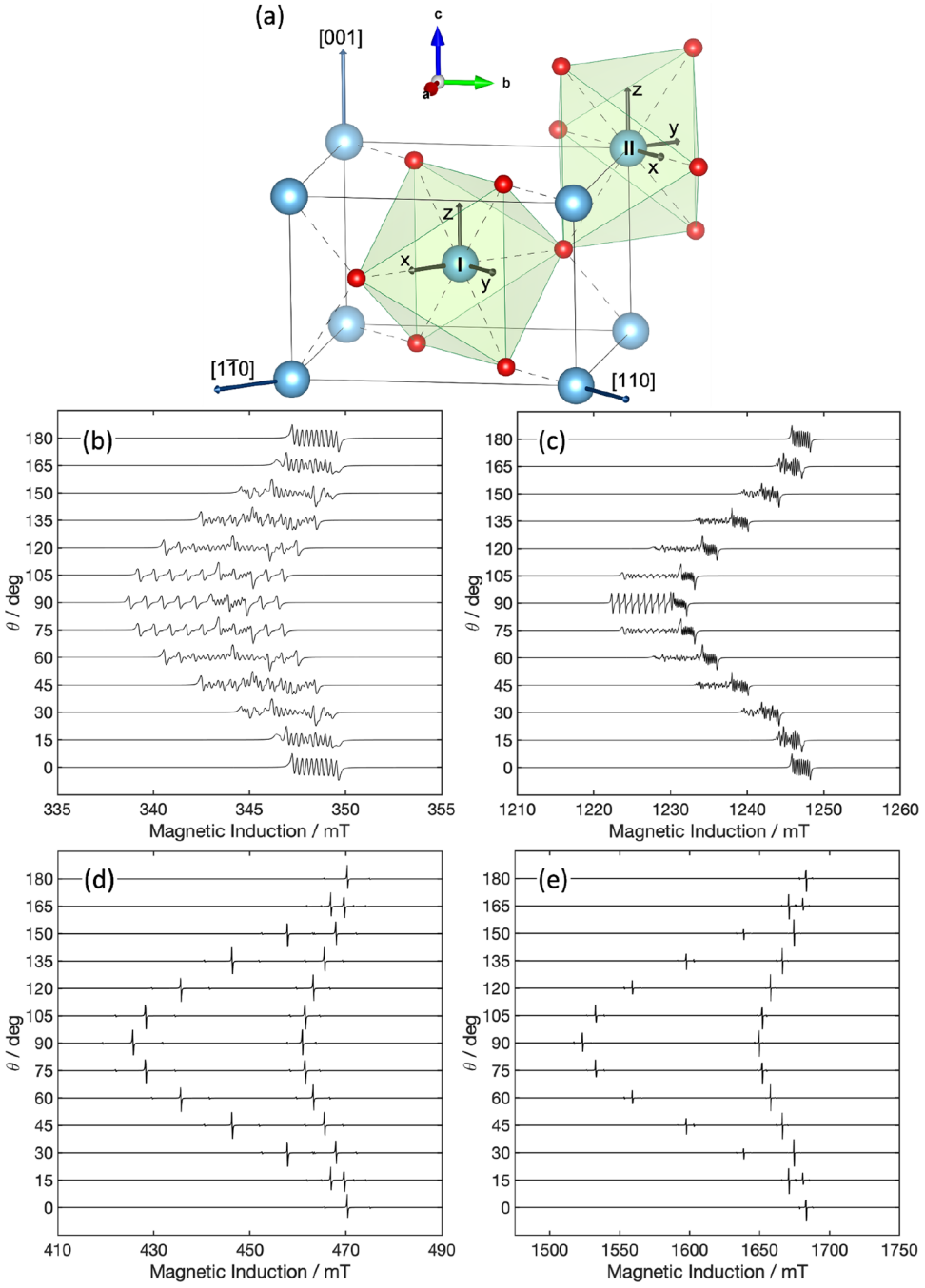

Figure 2. (a) Tetragonal crystal structure of rutile TiO_2 with two inequivalent Ti atoms (I and II). (b)−(e) Simulated angular dependency of the rutile single-crystal EPR spectra at 4.2 K for Nb^{4+} centers at (b) X-band and (c) Q-band; and W^{5+} centers at (d) X-band and (e) Q-band.

Table 1. Spin Hamiltonian Parameters of Reduced Dopant Metal Centers Detected in Nb^{5+} and W^{6+} Doped TiO_2.[a]

Reduced metal center	TiO_2 polymorph	g_x	g_y	g_z	A_x (MHz)	A_y (MHz)	A_z (MHz)	Reference
Nb^{4+}	rutile	1.970	1.985	1.941	n.d.	n.d.	n.d.	This work
Nb^{4+}	rutile	1.973	1.981	1.948	5.0	23.8	7.0	48
W^{5+}	rutile	1.594	1.473	1.443	277.5	122.4	191.1	This work
W^{5+}	rutile	1.5944	1.4725	1.4431	277.3	122.3	191.0	49

[a] x, y, and z are here along [1$\bar{1}$0], [110], and [001], respectively. [001] corresponds to the rutile crystal c-axis (see also Figure 2).

resonance observations in terms of the energetics of intraband gap states, we relied on self-consistent DFT+U calculations in an NAO framework, given that constrained DFT+U calculations could not rationalize our experimental observations (see SI Section S1.3.2). The total density of states (TDOS) reported in Figure 3a,c shows defect states pinned to the bottom of the TiO_2 conduction band for both anatase NTO and WTO, respectively, in perfect agreement with our

https://doi.org/10.1021/acs.jpcc.5c04364
J. Phys. Chem. C 2025, 129, 15453−15461

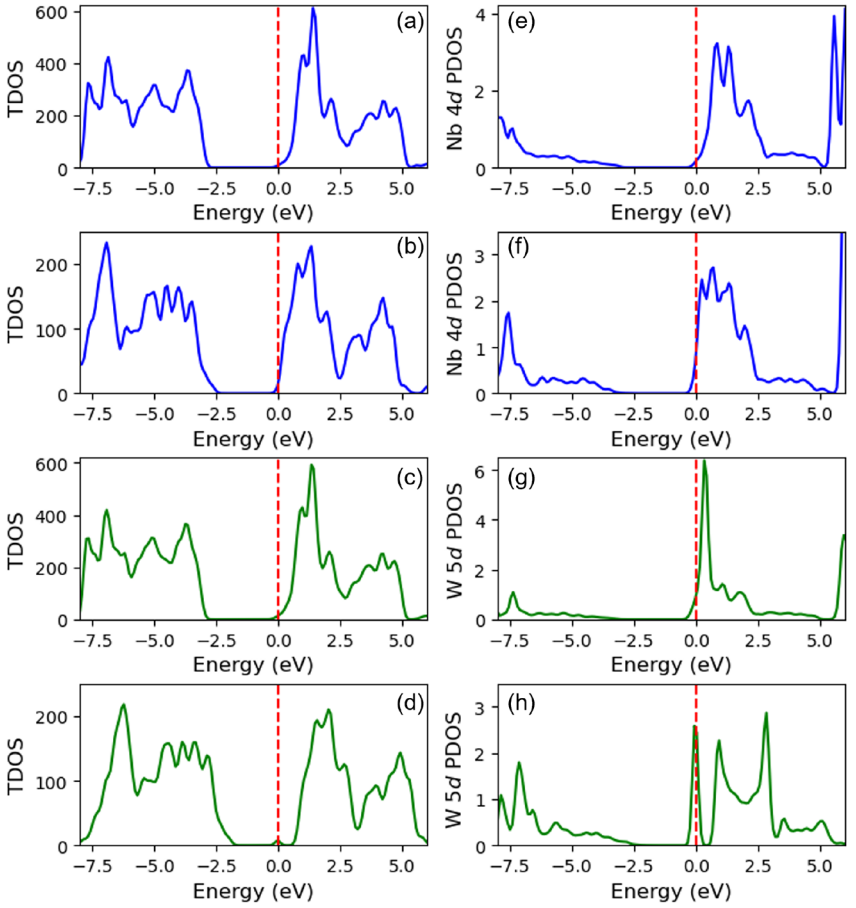

Figure 3. Self-consistent DFT+*U*-predicted TDOS and PDOS for anatase NTO ((a) and (e), respectively), anatase WTO ((b) and (f), respectively), rutile NTO ((c) and (g), respectively), and rutile WTO ((d) and (h), respectively). All TDOS and PDOS are plotted relative to the Fermi level indicated by the red dashed line.

EPR observations for NTO-A and WTO-A. From the corresponding projected density of states (PDOS) in Figure 3e,g, there are small Nb 4*d* and W 5*d* signatures at the Fermi level indicating these states are partially delocalized over Ti sites, contributing to metallic-type behavior. On the other hand, self-consistent DFT+*U* calculations show that the Nb 4*d* signature in rutile NTO is an order of magnitude greater at the Fermi level than in anatase NTO, when normalizing with respect to the different defect concentrations in our simulation supercells, as shown in the PDOS in Figure 3e,f.

These results can be attributed to differences in the filling of the five Nb 4*d* orbitals, notably, the greater occupancy of the three t_{2g} orbitals in rutile NTO, which correspond to orbital magnetic quantum numbers $m_l = -2, -1$, and 1[29] in Figure 4. There is a negligible difference in the trace of the Nb 4*d* occupation matrix (*i.e.*, the total Nb 4*d* subshell occupancy) in anatase NTO (1.48) compared with that of rutile NTO (1.49). Figure 3d,h show the TDOS and W 5*d* PDOS for the rutile WTO, respectively. Here, a localized W 5*d* midgap state is predicted at ca. 0.7 eV below the TiO_2 conduction band. The character of the midgap state is W $5d_{z^2}$, corresponding to a large occupation number of 0.93 for the $m_l = 0$ orbital in the W 5*d* occupation matrix (Figure 4). The other diagonal terms of the W 5*d* occupation matrix are of similar magnitude in anatase WTO and rutile WTO, which suggests the formation of W^{5+} in rutile but not in anatase.

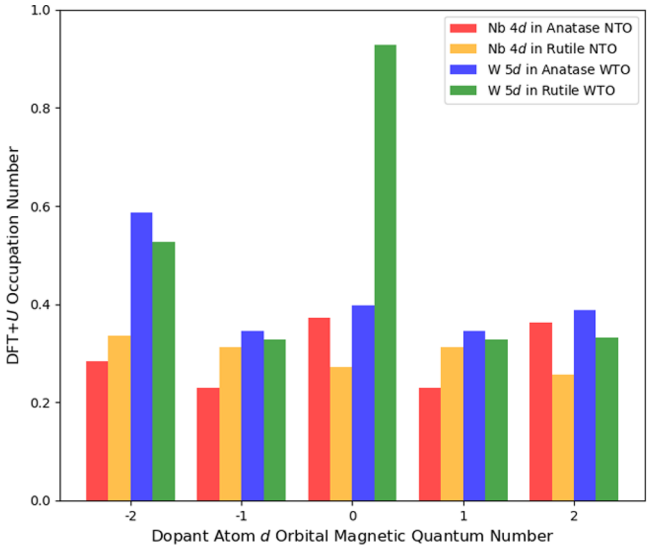

Figure 4. Ground-state orbital occupation numbers for Nb 4*d* and W 5*d* in doped anatase and rutile TiO_2 calculated using self-consistent DFT+*U*.

The formation of W^{5+} in rutile WTO is also suggested based on the local lattice distortion surrounding the W dopant, which is associated with localized polaronic states in defective TiO_2,[51,52] as shown in Figure 5, which plots the change in

https://doi.org/10.1021/acs.jpcc.5c04364
J. Phys. Chem. C 2025, 129, 15453−15461

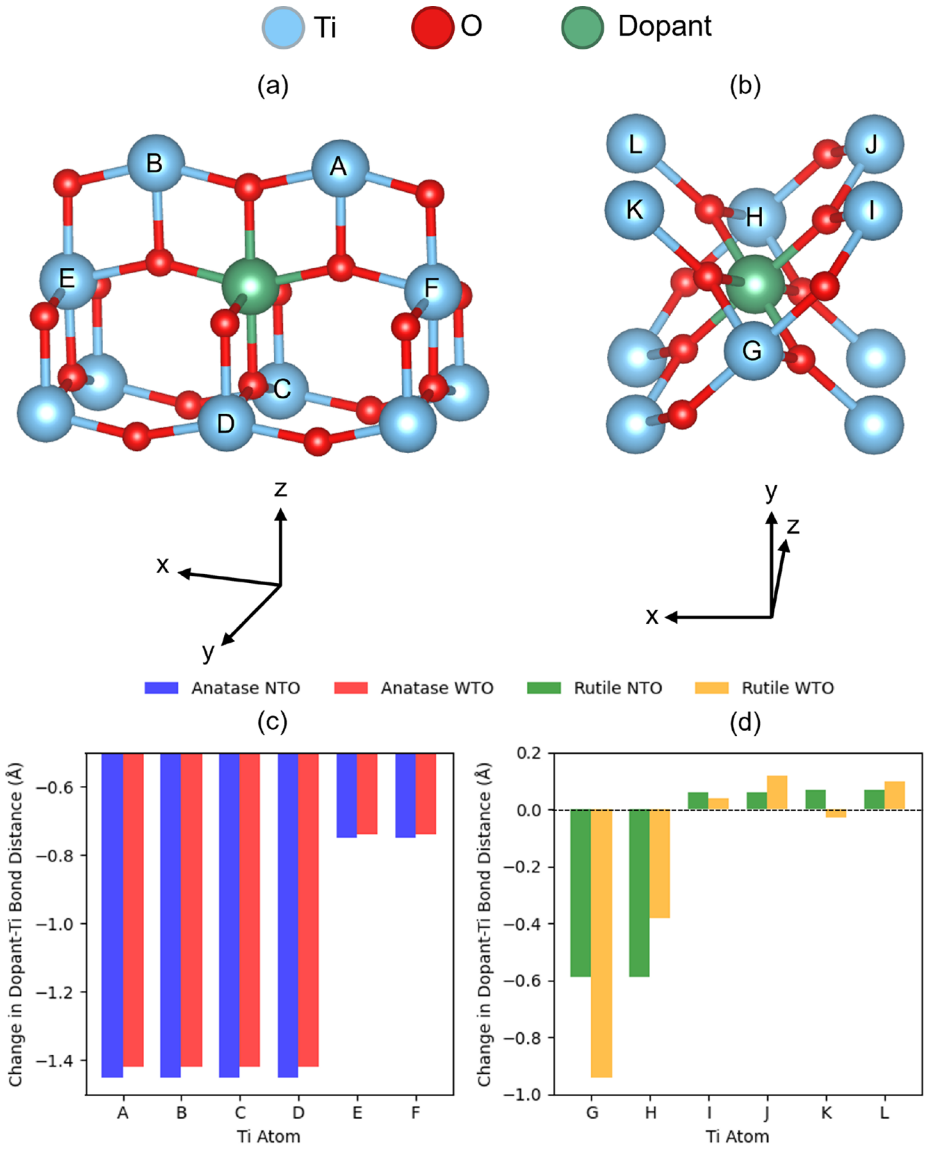

Figure 5. Change in the self-consistent DFT+*U*-calculated bond distances between the dopant atom and surrounding Ti atoms in doped anatase (atoms A−F in (a)) and doped rutile (atoms G−L in (b)) calculated relative to the average Ti−Ti bond distance in bulk anatase (c) and rutile (d) TiO_2.

the bond distance between the dopant atom and six neighboring Ti atoms relative to the average Ti−Ti bond distance in bulk anatase and rutile TiO_2. Figure 5c shows symmetric geometric relaxation around the substitutional defect in anatase NTO and WTO, where the change in bond length between the dopant atom and Ti atoms A−D is almost constant for both materials, as is the change in bond length with Ti atoms E and F. In Figure 5d, there is a stronger asymmetric local lattice distortion around the dopant atom in rutile WTO compared to that in rutile NTO, as shown by the differences in the change in bond lengths between the dopant atom and Ti atoms G-L.

4. CONCLUSIONS

NTO and WTO are promising TCOs with applications in heterogeneous photocatalysis and high-efficiency photovoltaics and electronics. However, there remains uncertainty in the atomistic mechanisms that govern charge compensation in these materials, which prevents the development of accurate structure−property models for material optimization. Using EPR spectroscopy, charge compensation is shown as highly sensitive to the TiO_2 polymorph, with Nb^{4+} and W^{5+} signals present in substitutionally doped rutile but not in doped anatase. The observations are complemented by contemporary DFT+*U* calculations in an all-electron NAO framework, for which self-consistent resolution of the Ti 3*d*, Nb 4*d*, and W 5*d* orbital occupancies is crucial. Self-consistent DFT+*U* predicts the favorability of Nb^{4+} in rutile NTO through greater filling of the Nb 4*d* t_{2g} orbitals and reduced filling of the e_g orbitals compared to anatase NTO. Self-consistent DFT+*U* also predicts W^{5+} in rutile WTO through the formation of a localized midgap state of $5d_{z^2}$ character that is not formed in anatase WTO. Our approach and findings provide a coherent view on the reducibility of metal centers in semiconducting TiO_2, matching experiments and theory without apparent disagreement, while also providing a clear understanding of how the reducibility of metal centers and electron trapping energetics in TiO_2 are polymorph-dependent. The improved

https://doi.org/10.1021/acs.jpcc.5c04364
J. Phys. Chem. C 2025, 129, 15453−15461

fundamental understanding enables precise control over the electronic and magnetic properties of transition-metal-doped TiO_2, advancing the rational design of high-performance materials for energy conversion and catalytic applications.

■ ASSOCIATED CONTENT

Data Availability Statement

The input and output files of all electronic structure calculations have been uploaded as a data set to the NOMAD repository at doi: 10.17172/NOMAD/2024.09.04-1.

Supporting Information

The Supporting Information is available free of charge at https://pubs.acs.org/doi/10.1021/acs.jpcc.5c04364.

Section S1, electronic structure calculations; and Section S2, powder XRD characterization (PDF)

■ AUTHOR INFORMATION

Corresponding Author

Andrea Folli − *Cardiff Catalysis Institute, School of Chemistry, Translational Research Hub and Net Zero Innovation Institute, Cardiff Catalysis Institute, School of Chemistry, Translational Research Hub, Cardiff University, Cardiff CF24 4HF, U.K.;* orcid.org/0000-0001-8913-6606; Email: FolliA@cardiff.ac.uk

Authors

Amit Chaudhari − *Cardiff Catalysis Institute, School of Chemistry, Translational Research Hub, Cardiff University, Cardiff CF24 4HF, U.K.*

Andrew J. Logsdail − *Cardiff Catalysis Institute, School of Chemistry, Translational Research Hub, Cardiff University, Cardiff CF24 4HF, U.K.;* orcid.org/0000-0002-2277-415X

Complete contact information is available at: https://pubs.acs.org/10.1021/acs.jpcc.5c04364

Author Contributions

A.F. and A.J.L. contributed to the conceptualization of the project and funding. A.J.L. and A.C. contributed to software choices and computational method development in this work. A.C. performed the electronic structure calculations presented in this work. A.F. performed the EPR spectroscopy and related simulations presented in this work. All authors contributed to the analysis of results and preparation of the manuscript.

Notes

The authors declare no competing financial interest.

■ ACKNOWLEDGMENTS

The authors thank Harald Oberhofer, Matthias Kick, and Maximilian Brand for valuable scientific discussions regarding the implementation of DFT+*U* in FHI-aims. The authors acknowledge funding by the Prosperity Partnership project Sustainable Catalysis for Clean Growth, funded by the UK Engineering and Physical Sciences Research Council (EPSRC), bp, through the bp International Centre for Advanced Materials (bp-ICAM) and Johnson Matthey plc in collaboration with Cardiff University and The University of Manchester (EPSRC grant number EP/V056565/1). A.F. acknowledges the Cardiff University Net Zero Innovation Institute for funding a University Research Fellowship at the Cardiff Catalysis Institute. A.J.L. acknowledges funding by the UKRI Future Leaders Fellowship program (MR/T018372/1 and MR/Y034279/1). The authors acknowledge computational resources and support from the Supercomputing Wales project, which is part-funded by the European Regional Development Fund (ERDF) *via* the Welsh Government; and the UK National Supercomputing Services ARCHER and ARCHER2, accessed *via* membership of the Materials Chemistry Consortium, which is funded by the Engineering and Physical Sciences Research Council (EP/L000202/1, EP/R029431/1, and EP/T022213/1).

■ REFERENCES

(1) Furubayashi, Y.; Hitosugi, T.; Yamamoto, Y.; Inaba, K.; Kinoda, G.; Hirose, Y.; Shimada, T.; Hasegawa, T. A transparent metal: Nb-doped anatase TiO_2. *Appl. Phys. Lett.* **2005**, *86*, 252101.

(2) Zhang, S. X.; Kundaliya, D. C.; Yu, W.; Dhar, S.; Young, S. Y.; Salamanca-Riba, L. G.; Ogale, S. B.; Vispute, R. D.; Venkatesan, T. Niobium doped TiO_2: Intrinsic transparent metallic anatase versus highly resistive rutile phase. *J. Appl. Phys.* **2007**, *102*, No. 013701.

(3) Lee, S.; Noh, J. H.; Han, H. S.; Yim, D. K.; Kim, D. H.; Lee, J. kun; Kim, J. Y.; Jung, H. S.; Hong, K. S. Nb-Doped TiO_2: A New Compact Layer Material for TiO_2 Dye-Sensitized Solar Cells. *J. Phys. Chem. C* **2009**, *113*, 6878−6882.

(4) Tasaki, C.; Oka, N.; Yagi, T.; Taketoshi, N.; Baba, T.; Kamiyama, T.; Nakamura, S. ichi; Shigesato, Y. Thermophysical Properties of Transparent Conductive Nb-Doped TiO_2 Films. *Jpn. J. Appl. Phys.* **2012**, *51*, No. 035802.

(5) Lee, H. Y.; Robertson, J. Doping and compensation in Nb-doped anatase and rutile TiO_2. *J. Appl. Phys.* **2013**, *113*, 213706.

(6) De Trizio, L.; Buonsanti, R.; Schimpf, A. M.; Llordes, A.; Gamelin, D. R.; Simonutti, R.; Milliron, D. J. Nb-Doped Colloidal TiO_2 Nanocrystals with Tunable Infrared Absorption. *Chem. Mater.* **2013**, *25*, 3383−3390.

(7) Park, J. T.; Chi, W. S.; Jeon, H.; Kim, J. H. Improved electron transfer and plasmonic effect in dye-sensitized solar cells with bi-functional Nb-doped TiO_2/Ag ternary nanostructures. *Nanoscale* **2014**, *6*, 2718−2729.

(8) Biedrzycki, J.; Livraghi, S.; Giamello, E.; Agnoli, S.; Granozzi, G. Fluorine- and Niobium-Doped TiO_2: Chemical and Spectroscopic Properties of Polycrystalline n-Type-Doped Anatase. *J. Phys. Chem. C* **2014**, *118*, 8462−8473.

(9) Folli, A.; Bloh, J. Z.; Walker, R.; Lecaplain, A.; Macphee, D. E. Properties and Photochemistry of Valence-Induced-Ti^{3+} Enriched (Nb,N)-Codoped Anatase TiO_2 Semiconductors. *Phys. Chem. Chem. Phys.* **2015**, *17*, 4849−4853.

(10) Yue, J.; Suchomski, C.; Voepel, P.; Ellinghaus, R.; Rohnke, M.; Leichtweiss, T.; Elm, M. T.; Smarsly, B. M. Mesoporous niobium-doped titanium dioxide films from the assembly of crystalline nanoparticles: study on the relationship between the band structure, conductivity and charge storage mechanism. *J. Mater. Chem. A* **2017**, *5*, 1978−1988.

(11) Phipps, G.; Mikolajczak, C.; Guckes, T. Indium and Gallium: long-term supply. *Renew. Energy Focus* **2008**, *9*, 56−59.

(12) Green, M. A. The Path to 25% Silicon Solar Cell Efficiency: History of Silicon Cell Evolution. *Prog. Photovolt: Res. Appl.* **2009**, *17*, 183−189.

(13) Vesborg, P. C. K.; Jaramillo, T. F. Addressing the terawatt challenge: scalability in the supply of chemical elements for renewable energy. *RSC Adv.* **2012**, *2*, 7933.

(14) Lokanc, M.; Eggert, R.; Redlinger, M. *The Availability of Indium: The Present, Medium Term, and Long Term*, **2015**, www.nrel.gov/publications.\%0Awww.nrel.gov/publications.\%0Ahttps://www.nrel.gov/docs/fy16osti/62409.pdf.

(15) Chen, D.-m.; Xu, G.; Miao, L.; Chen, L.-h.; Nakao, S.; Jin, P. W-doped anatase TiO_2 transparent conductive oxide films: Theory and experiment. *J. Appl. Phys.* **2010**, *107*, No. 063707.

(16) Hou, Q.; Zhao, C.; Guo, S.; Mao, F.; Zhang, Y. Effect on electron structure and magneto-optic property of heavy W-doped anatase TiO_2. *PLoS One* **2015**, *10*, No. e0122620.

(17) Wang, H.; Zhao, C.; Yin, L.; Li, X.; Tu, X.; Lim, G.; Liu, Y.; Zhao, Z. W-doped TiO_2 as electron transport layer for high performance solution-processed perovskite solar cells. *Appl. Surf. Sci.* **2021**, *563*, No. 150298.
(18) Wang, H. Y.; Yang, H.; Zhang, L.; Chen, J.; Liu, B. Niobium Doping Enhances Charge Transport in TiO_2 Nanorods. *ChemNanoMat* **2016**, *2*, 660−664.
(19) Wang, H. Y.; Chen, J.; Xiao, F. X.; Zheng, J.; Liu, B. Doping-induced structural evolution from rutile to anatase: Formation of Nb-doped anatase TiO_2 nanosheets with high photocatalytic activity. *J. Mater. Chem. A* **2016**, *4*, 6926−6932.
(20) Santos, E.; Catto, A. C.; Peterline, A. F.; Avansi, W. Transition metal (Nb and W) doped TiO_2 nanostructures: The role of metal doping in their photocatalytic activity and ozone gas-sensing performance. *Appl. Surf. Sci.* **2022**, *579*, No. 152146.
(21) Sathasivam, S.; Bhachu, D. S.; Lu, Y.; Chadwick, N.; Althabaiti, S. A.; Alyoubi, A. O.; Basahel, S. N.; Carmalt, C. J.; Parkin, I. P. Tungsten Doped TiO_2 with Enhanced Photocatalytic and Optoelectrical Properties *via* Aerosol Assisted Chemical Vapor Deposition. *Sci. Rep.* **2015**, *5*, 10952.
(22) Folli, A.; Bloh, J. Z.; Armstrong, K.; Richards, E.; Murphy, D. M.; Lu, L.; Kiely, C. J.; Morgan, D. J.; Smith, R. I.; Mclaughlin, A. C.; Macphee, D. E. Improving the Selectivity of Photocatalytic NOx Abatement through Improved O2 Reduction Pathways Using Ti0.909W0.091O2Nbx Semiconductor Nanoparticles: From Characterization to Photocatalytic Performance. *ACS Catal.* **2018**, *8*, 6927−6938.
(23) Hitosugi, T.; Kamisaka, H.; Yamashita, K.; Nogawa, H.; Furubayashi, Y.; Nakao, S.; Yamada, N.; Chikamatsu, A.; Kumigashira, H.; Oshima, M.; Hirose, Y.; Shimada, T.; Hasegawa, T. Electronic band structure of transparent conductor: Nb-doped anatase TiO_2. *Appl. Phys. Express* **2008**, *1*, No. 111203.
(24) Ghuman, K. K.; Singh, C. V. A DFT + *U* study of (Rh, Nb)-codoped rutile TiO_2. *J. Phys.: Condens. Matter.* **2013**, *25*, No. 085501.
(25) Morgan, B. J.; Scanlon, D. O.; Watson, G. W. Small polarons in Nb- and Ta-doped rutile and anatase TiO_2. *J. Mater. Chem.* **2009**, *19*, 5175−5178.
(26) Raghav, A.; Hongo, K.; Maezono, R.; Panda, E. Electronic structure and effective mass analysis of doped TiO_2 (anatase) systems using DFT + *U*. *Comput. Mater. Sci.* **2022**, *214*, No. 111714.
(27) Belošević-Čavor, J.; Koteski, V.; Umićević, A.; Ivanovski, V. Effect of 5*d* transition metals doping on the photocatalytic properties of rutile TiO_2. *Comput. Mater. Sci.* **2018**, *151*, 328−337.
(28) Kick, M.; Reuter, K.; Oberhofer, H. Intricacies of DFT+*U*, Not Only in a Numeric Atom Centered Orbital Framework. *J. Chem. Theory Comput.* **2019**, *15*, 1705−1718.
(29) Allen, J. P.; Watson, G. W. Occupation matrix control of *d*- and *f*-electron localisations using DFT+*U*. *Phys. Chem. Chem. Phys.* **2014**, *16*, 21016−21031.
(30) Doebelin, N.; Kleeberg, R. Profex: A graphical user interface for the Rietveld refinement program BGMN. *J. Appl. Crystallogr.* **2015**, *48*, 1573−1580.
(31) Stoll, S.; Schweiger, A. EasySpin, a Comprehensive Software Package for Spectral Simulation and Analysis in EPR. *J. Magn. Reson.* **2006**, *178*, 42−55.
(32) Blum, V.; Gehrke, R.; Hanke, F.; Havu, P.; Havu, V.; Ren, X.; Reuter, K.; Scheffler, M. *Ab initio* molecular simulations with numeric atom-centered orbitals. *Comput. Phys. Commun.* **2009**, *180*, 2175−2196.
(33) Larsen, A. H.; Mortensen, J. J.; Blomqvist, J.; Castelli, I. E.; Christensen, R.; Dułak, M.; Friis, J.; Groves, M. N.; Hammer, B.; Hargus, C.; Hermes, E. D.; Jennings, P. C.; Jensen, P. B.; Kermode, J.; Kitchin, J. R.; Kolsbjerg, E. L.; Kubal, J.; Kaasbjerg, K.; Lysgaard, S.; Maronsson, J. B.; Maxson, T.; Olsen, T.; Pastewka, L.; Peterson, A.; Rostgaard, C.; Schiøtz, J.; Schütt, O.; Strange, M.; Thygesen, K. S.; Vegge, T.; Vilhelmsen, L.; Walter, M.; Zeng, Z.; Jacobsen, K. W. The atomic simulation environment—a Python library for working with atoms. *J. Phys.: Condens. Matter* **2017**, *29*, 273002.
(34) Lamiel-Garcia, O.; Ko, K. C.; Lee, J. Y.; Bromley, S. T.; Illas, F. When Anatase Nanoparticles Become Bulklike: Properties of Realistic TiO_2 Nanoparticles in the 1−6 nm Size Range from All Electron Relativistic Density Functional Theory Based Calculations. *J. Chem. Theory Comput.* **2017**, *13*, 1785−1793.
(35) Wellendorff, J.; Lundgaard, K. T.; Jacobsen, K. W.; Bligaard, T. mBEEF: An accurate semi-local Bayesian error estimation density functional. *J. Chem. Phys.* **2014**, *140*, 144107.
(36) Perdew, J. P.; Ruzsinszky, A.; Csonka, G. I.; Vydrov, O. A.; Scuseria, G. E.; Constantin, L. A.; Zhou, X.; Burke, K. Restoring the Density-Gradient Expansion for Exchange in Solids and Surfaces. *Phys. Rev. Lett.* **2008**, *100*, No. 136406.
(37) Lehtola, S.; Steigemann, C.; Oliveira, M. J.; Marques, M. A. Recent developments in libxc — A comprehensive library of functionals for density functional theory. *SoftwareX* **2018**, *7*, 1−5.
(38) Broyden, C. G. The Convergence of a Class of Double-rank Minimization Algorithms 1 General Considerations, IMA. *J. Appl.* **1970**, *6*, 76−90.
(39) Fletcher, R. A new approach to variable metric algorithms. *Comput. J.* **1970**, *13*, 317−322.
(40) Shanno, D. F. Conditioning of Quasi-Newton Methods for Function Minimization. *Math. Comput.* **1970**, *24*, 647−656.
(41) Goldfarb, D. A Family of Variable-Metric Methods Derived by Variational Means. *Math. Comput.* **1970**, *24*, 23−26.
(42) Birch, F. Finite Elastic Strain of Cubic Crystals. *Phys. Rev.* **1947**, *71*, 809−824.
(43) Kavan, L.; Grätzel, M.; Gilbert, S. E.; Klemenz, C.; Scheel, H. J. Electrochemical and Photoelectrochemical Investigation of Single-Crystal Anatase. *J. Am. Chem. Soc.* **1996**, *118*, 6716−6723.
(44) Arlt, T.; Bermejo, M.; Blanco, M. A.; Gerward, L.; Jiang, J. Z.; Olsen, J. S.; Recio, J. M. High-pressure polymorphs of anatase TiO_2. *Phys. Rev. B* **2000**, *61*, 14414.
(45) Jakob, K.; Oberhofer, H. *Master's thesis: Self-Consistency in the Hubbard-Corrected DFT+U Method*; Technical University of Munich: Faculty of Chemistry, 2021.
(46) Folli, A.; Bloh, J.; Beukes, E.-P.; Howe, R.; MacPhee, D. Photogenerated charge carriers and paramagnetic species in (W,N)-codoped TiO_2 photocatalysts under visible-light irradiation: An EPR study. *J. Phys. Chem. C* **2013**, *117*, 22149.
(47) Bloh, J. Z.; Folli, A.; Macphee, D. E. Adjusting Nitrogen Doping Level in Titanium Dioxide by Codoping with Tungsten: Properties and Band Structure of the Resulting Materials. *J. Phys. Chem. C* **2014**, *118*, 21281−21292.
(48) Zimmermann, P. H. Temperature Dependence of the EPR Spectra of Niobium-Doped TiO_2. *Phys. Rev. B* **1973**, *8*, 3917−3927.
(49) Chang, T. T. Paramagnetic-Resonance Spectrum of W^{5+} in Rutile (TiO_2). *Phys. Rev.* **1966**, *147*, 264−267.
(50) Kiwi, J.; Suss, J. T.; Szapiro, S. EPR spectra of niobium-doped TiO_2 and implications for water photocleavage processes. *Chem. Phys. Lett.* **1984**, *106*, 135−138.
(51) Lin, C.; Shin, D.; Demkov, A. A. Localized states induced by an oxygen vacancy in rutile TiO_2. *J. Appl. Phys.* **2015**, *117*, 225703.
(52) Yim, C. M.; Watkins, M. B.; Wolf, M. J.; Pang, C. L.; Hermansson, K.; Thornton, G. Engineering Polarons at a Metal Oxide Surface. *Phys. Rev. Lett.* **2016**, *117*, No. 116402.

https://doi.org/10.1021/acs.jpcc.5c04364
J. Phys. Chem. C 2025, 129, 15453−15461